

**LABORATORY TESTING OF MINERAL DETECTION AND ABUNDANCE ALGORITHMS: FACTOR ANALYSIS DETECTION AND NONLINEAR MIXTURE MODELING** J. F. Mustard<sup>1</sup>, J. D. Tarnas<sup>1</sup>, X. Wu<sup>1</sup>, E. Das<sup>1</sup>, and M. Parente<sup>2</sup>, <sup>1</sup>Department of Earth, Environmental and Planetary Sciences, Brown University, Providence RI 02912. (john\_mustard@brown.edu) <sup>2</sup>Dept. of Electrical and Computer Engineering, University of Massachusetts Amherst, MA 01003.

**Introduction:** We are testing advanced algorithms for mineral detection and abundance determination in the laboratory using mineral mixtures of known abundance and particle size. We measure these mixtures using a visible to short-wave infrared (i.e. 0.4-2.6  $\mu\text{m}$ ) hyperspectral imager [1]. Over the past decade, new approaches for mineral detection and abundance have emerged [2, 6] that are very promising, but have not been rigorously tested in laboratory settings. Specifically, laboratory testing is required to evaluate the fidelity of detection algorithms with imaging spectrometer data that exhibit signal to noise, structured noise, and other properties characteristics of imaging spectrometer data sets (e.g. CRISM, M3). In this phase of our ongoing investigations, we are presenting the experimental design in a companion abstract [1] and initial results of mineral detection methods (Factor Analysis/Target Transformation, FA/TT) and abundance determination with a Hapke nonlinear mixture model.

**Data Acquisition:** The experimental design and measurements are presented in [1]. A specially designed sample tray is loaded with binary mixtures of a target mineral mixed with the Exolith Mars Global Simulant (MGS-1) [4]. The loaded sample tray is measured with the Brown University Visible-Shortwave Infrared Headwall Imaging Spectrometer. The imaging spectrometer consists of a visible-near infrared and a short-wave infrared component, bore-sighted through the same fore optics. Together they provide optical observations across the wavelength range 400 – 2600 nm [1].

The spectrometer is fixed 25 cm above a translation table giving a pixel size of  $<0.071$  mm in the visible-near infrared (VNIR) (0.38-1.01  $\mu\text{m}$ ) and  $\sim 0.339$  mm in the shortwave infrared (SWIR) (0.95-2.6  $\mu\text{m}$ ). We have collected imaging spectrometer data of over 8 mixture suites, but are presenting the preliminary results of just the mixtures of selenite (gypsum) and MGS-1.

**Analysis Methods: (1) Mineral Abundance** At VNIR-SWIR wavelengths, multiple scattering leads to nonlinear spectral mixing systematics [5, 6, 7]. Linearization is achieved by converting reflectance to single-scattering albedo [6]. Here we apply the most simple nonlinear spectral mixture analysis [8] where the endmember spectra are known and generated from the imaging spectrometer data. Mineral abundance is a fundamental goal of our work and we will employ more advanced approaches [e.g. 1] in future work. In this test, endmembers for selenite and MGS are extracted from

the imaging spectrometer data and used to unmix the scene along with a neutral 100% white endmember. The preliminary results are shown in Figure 1 and Table 1.

The simplified Hapke model [8] is able to estimate the abundance of selenite in binary mixtures with MGS to within 5% for mixtures with 5% or more of selenite. The mixtures with  $<5\%$  selenite are not distinguishable from the blanks (pure MGS-1). We will compare this performance with other target minerals such as carbonate and serpentine.

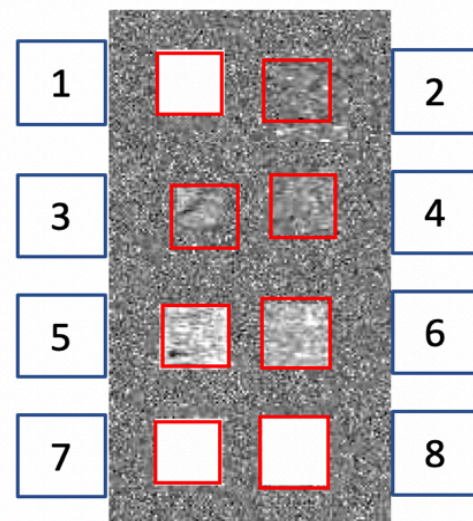


Figure 1. Fractional abundance of selenite from nonlinear mixture modeling. Red boxes show where abundance information was extracted for Table 1.

Table 1: Fractional abundance of Selenite and MGS from nonlinear mixture modeling results in Figure 1. The numbers are averages with SD over the red boxes in Figure 1.

% Sel	Fig. 1 Box #	Model Selenite%	MGS%	RMS
0	2	0.017 $\pm$ 0.01	0.978 $\pm$ 0.01	0.004
1	3	0.031 $\pm$ 0.03	0.946 $\pm$ 0.02	0.005
2	4	0.034 $\pm$ 0.03	0.946 $\pm$ 0.01	0.005
5	6	0.063 $\pm$ 0.02	0.915 $\pm$ 0.03	0.005
10	5	0.070 $\pm$ 0.03	0.912 $\pm$ 0.04	0.005
20	8	0.245 $\pm$ 0.03	0.714 $\pm$ 0.04	0.009
50	7	0.545 $\pm$ 0.01	0.414 $\pm$ 0.01	0.015
100	1	1.114 $\pm$ 0.22	-0.12 $\pm$ 0.24	0.004

**Analysis Methods: (2) Mineral Detection** has commonly been determined by leveraging diagnostic absorption features, keying on the position, strength and shape of absorptions in remote and laboratory spectra using spectral parameters [9] to guide the selection of

remotely acquired spectra, which are then compared to laboratory spectra [e.g. 10, 11, 12]. However, this approach requires a pre-determination of likely minerals to be present, is not flexible or extendable to diverse situations, and can be severely hampered by instrument noise and calibration artifacts.

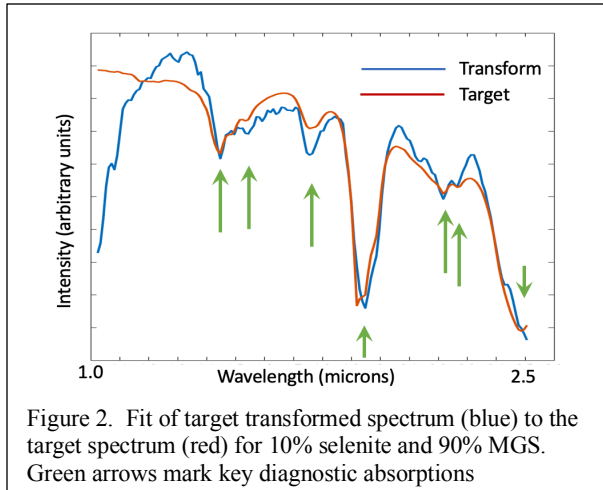


Figure 2. Fit of target transformed spectrum (blue) to the target spectrum (red) for 10% selenite and 90% MGS. Green arrows mark key diagnostic absorptions

Factor Analysis and Target Transformation (FATT) [13] is a statistical technique to identify the presence of minerals in hyperspectral data based on their spectral signatures. It is predicated on the principle that a mineral present in variable abundance across a scene will impart variance to a hyperspectral data set. Eigenvalues and eigenvectors from 10s to 1000s of pixels from a hyperspectral imaging data set are determined. A target spectrum is presented and the eigenvectors are linearly fit to the target spectrum, creating the transform spectrum. If the transform spectrum matches the target spectrum to a defined metric of measure (e.g. Root Mean Square Error or spectral angle) then there is a high likelihood the material represented by that target spectrum exists in the hyperspectral data set [13]. It is unknown at this time the minimum number of eigenvectors needed for the transform (this likely varies instrument-to-instrument), the target mineral abundance detection limits, and the rate of false positive detections. One of our goals is to use the laboratory data described in [1] to rigorously determine the number of eigenvectors required, appropriate metrics for goodness of fit and factors leading to false positive or missed identifications.

An important limitation of some FATT applications is that the exact location in a data set with the target mineral spectral signature cannot be determined. To overcome this limitation, we developed a variant we call Dynamic Aperture FATT (DAFA/TT), explained in [14], to define the most likely locations in the hyperspectral data set where the target mineral is concentrated. We applied DAFA/TT to the selenite /MGS mixture data and the results are shown in Figures 2 and 3.

Figure 2 shows a typical validated detection where all the diagnostic absorptions for selenite are reproduced in the transform spectrum. The fit in Fig. 2 is for cluster 3 in Fig. 3 (10% selenite and 90% MGS), which was generated by DAFA/TT application to the entire image. The algorithm was applied to the same data used for abundance mapping (Figure 1) to produce an automated detection map for selenite (Figure 3).

Areas in magenta are valid detections and they map areas of the hyper-

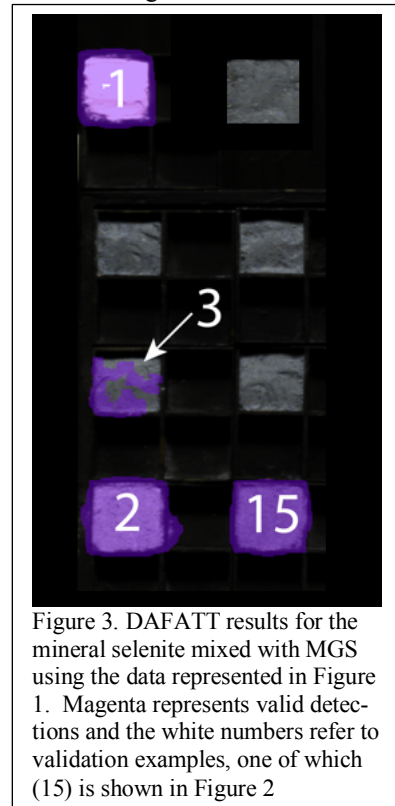


Figure 3. DAFA/TT results for the mineral selenite mixed with MGS using the data represented in Figure 1. Magenta represents valid detections and the white numbers refer to validation examples, one of which (15) is shown in Figure 2

spectral data that contain 10% or more selenite mixed with MGS. We used a simple 15 eigenvector-limit fit and are evaluating how to maximize and automate the eigenvector number determination. The rate of false detections in this and other approaches is also being investigated [15]. Both the mixture modeling and DAFA/TT methods confidently resolve selenite mixed

with MGS at 10% abundance or greater. More detailed applications across a broader range of minerals mixed with MGS will be presented at the meeting.

**References:** [1] Das, E., et al., LPSC (2020) [2] Thomas, N. H., and J. L. Bandfield. *Icarus* 291 (2017): 124-135. [4] Cannon, K. M., et al. *Icarus* 317 (2019): 470-478. [5] Keshava N. and Mustard J.F. (2002), *IEEE Signal Processing Magazine*, DOI: 10.1109/79.974727 [6] Lapotre, M., et al. (2017), *J. Geophys. Res.-Planets*, 10.1002/2016JE005133. [7] Hapke B., *Theory of reflectance and emittance spectroscopy*, Cambridge University Press (2012)[8] Mustard, J. F. and Pieters, C. M., *JGR Planets* (1987). [9] Viviano-Beck, C. E., F. P. Seelos, S. L. Murchie, E. G. Kahn, K. D. Seelos, H. W. Taylor, K. Taylor et al. *J. of Geophys. Res.-Planets* 119, no. 6 (2014): 1403-1431. [10] Mustard, J. F., et al., *Nature* 454.7202 (2008): 305. [11] Pieters, C. M., et al. *Science* 326.5952 (2009): 568-572. [12] Ellmann, B. L. and C. S. Edwards, *Geology* 43, no. 10 (2015): 863-866. 2015. [14] Lin H., Tarnas J. D., Mustard J. F., Zhang X. Wu, X, LPSC 49, 2018. [15] Wu, X., et al., LPSC (2020)